High efficiency water splitting photoanodes composed of nano-structured anatase-rutile TiO_2 heterojunctions by pulsed-pressure MOCVD

Aleksandra J. Gardecka,[a] Catherine Bishop,[a] Darryl Lee,[b] Sacha Corby,[d] Ivan P. Parkin,[c] Andreas Kafizas[d]* and Susan Krumdieck[a]*

[a]Department of Mechanical Engineering, University of Canterbury, Christchurch, 8041, New Zealand

[b] Koti Technologies Limited, Christchurch, New Zealand

[c]Materials Chemistry Centre, Department of Chemistry, University College London, 20 Gordon Street, London, WC1H 0AJ, UK

[d]Department of Chemistry, Imperial College London, South Kensington, London, SW7 2AZ, UK

*corresponding authors: a.kafizas@imperial.ac.uk, susan.krumdieck@canterbury.ac.nz

ABSTRACT

In this article, thin solid films are processed *via* pulsed-pressure metal organic chemical vapour deposition (PP-MOCVD) on FTO substrates over a range of processing times to produce a range of thicknesses and microstructures. The films are highly nanostructured anatase-rutile TiO_2 composite films with unique single crystal dendrites. After annealing, carbon was removed, and materials showed improved water splitting activity; with IPCEs above 80 % in the UV, photocurrents of ~1.2 $mA.cm^{-2}$ at 1.23 V_{RHE} at 1 sun irradiance and an extension of photoactivity into the visible range. The annealed material exhibits minimal recombination losses and IPCEs amongst the highest reported in the literature; attributed to the formation of a high surface area nanostructured material and synergetic interactions between the anatase and rutile phases.

KEYWORDS

Titanium dioxide (TiO_2), anatase-rutile heterojunctions, solar water splitting, nanostructured photoelectrodes, PP-MOCVD,

INTRODUCTION

The extraction and combustion of more than 500 Gigatons of fossil carbon over the past 70 years has resulted in a build-up of CO_2 in the atmosphere that is causing global warming, and has driven research in alternative energy technologies that can ameliorate the effects of global warming [1, 2]. Solar photovoltaic cells directly produce electricity from renewable, but intermittent solar radiation. The intermittency of increased solar and wind generation is driving a search for energy storage solutions [3]. Fujishima and Honda, first demonstrated water splitting on a TiO_2 photoelectrode using UV light [4]. Research on the photoelectrochemical water splitting has been focused on improving device efficiency, enhancing the utilization of visible spectrum radiation, and achieving commercial viability[5, 6].

Photoelectrochemical water splitting is the process of decomposing water into oxygen and hydrogen on a semiconductor photocatalyst by light and an applied voltage [7]. The ultra-bandgap absorption of light results in the generation of electron hole pairs in the photocatalyst. The applied voltage assists the spatial separation of electron hole pairs, and these charge carriers participate in redox reactions at the semiconductor/electrolyte interface.

$$4H^+ + 4e^- \rightarrow 2H_2, \quad E^{\ominus} = 0\ V \qquad \text{(Eq 1a)}$$

$$2H_2O + 4h^+ \rightarrow O_2 + 4H^+, \quad E^{\ominus} = 1.23\ V \qquad \text{(Eq 1b)}$$

The conduction band should be sufficiently reducing for water reduction and hydrogen production to occur (Eq. 1a). The valence band should be sufficiently oxidising for water oxidation and the formation of oxygen to occur (Eq 1b) [8, 9]. The bandgap of the material should be wide enough to surpass the thermodynamic potential for water splitting (1.23 V) and additional kinetic barriers [10, 11].

Several research groups have focussed on improving the visible light activity and efficiency of water splitting materials [9, 12]. One of the most common strategies for improving the efficiency is to introduce nanostructure, which decouples the problem of long light absorption depths and poor minority carrier diffusion lengths [13]. Hole carrier diffusion lengths in TiO_2 are on the order of 10's of nanometres [14], and for these carriers to reach the semiconductor/electrolyte interface and oxidise water, they need to be formed near the material surface. By introducing nanostructures, such as pillars and rods, more holes are formed near the surface of the material, and higher water splitting efficiencies have been demonstrated [15, 16]. The studies to date have mainly used hydrothermal processing methods to synthesise TiO_2-based photoelectrodes [15, 17, 18]. The clear gap in the research and development of efficient and viable photoanodes for solar hydrogen production is in the area of upscalable processing methods to robust and stable photoelectrode materials.

In this paper we use the pulsed-pressure metal organic chemical vapour deposition (PP-MOCVD) method to produce nanostructured TiO_2 photoelectrodes from single-liquid source precursor solution of titanium tetra isopropoxide (TTIP) in toluene. Atmospheric

pressure CVD is used to produce TiO_2 thin films during the float glass manufacture process, which has resulted in the commercialisation of numerous "self-cleaning" products including Activ™, Bioclean™, Sunclean™ and Variclean™ [19, 20]. Control of precursor arrival rate and substrate temperature provides the control of microstructure [21]. In this study, we show that by controlling the deposition time by adjusting the number of pulses, we can produce a range of film thickness, fraction of anatase and rutile phases, and film topography.

In this article, we also study the role of co-deposited carbon, and its impact on the water splitting activity of our TiO_2 photoelectrodes. We find that highly nanostructured TiO_2 architectures, produced by pulsed-pressure metal organic chemical vapour deposition (PP-MOCVD), that contain both anatase and rutile phases, can achieve high water splitting efficiencies with minimal recombination losses (incident photon-to-current efficiencies up to 80 % in the UV). We believe that this upscalable synthetic route, and strategy for introducing nanostructure, can be applied to other materials systems that can harness more of the solar spectrum, and thus show potential enhancements in solar water splitting activity.

EXPERIMENTAL

Synthesis of TiO_2 photoanodes

TiO_2 films were grown using a pulsed pressure metal organic chemical vapour deposition (PP-MOCVD) process in a cold wall reactor, described previously by Lee *et al* [22]. The deposition temperature was measured by k-type thermocouple inserted into the susceptor and heated by an induction coil. Depositions were carried out on F: SnO_2 TEC Glass™ (13 Ω/□; 13 mm × 6 mm × 18 mm). The temperature was maintained at 525 °C for the entirety of the

deposition. A metered volume of precursor liquid solution (5 mol% solution of titanium tetra-isopropoxide (toluene, 500 μl per pulse) is directly injected through an ultrasonic atomizing nozzle into the continuously evacuated reactor volume at timed intervals, resulting in a sharp pressure pulse followed by pump-down. In the current reactor geometry, the susceptor is placed directly above an induction coil and the injector is located at the top of the reactor. The number of pulses was varied in each deposition resulting in films of varied thickness, anatase/rutile phase fractions and nanostructure (19, 92, 138, 184 and 460 pulses were investigated herein). The injection pulses were spaced 6 s apart. The chamber base pressure was held at 120 Pa, with the mean peak pressure in the region of 500 Pa. The effect of post-annealing was investigated, with samples annealed in air at 500 °C for 3 h.

Physical characterisation

X-ray diffraction (XRD) was carried out on the Bruker GADDS D8 diffractometer with a Cu K_α X-ray source over the range $10° < 2\theta < 66°$. X-ray diffraction was carried out with a glancing incident angle of 1.0° unless otherwise stated. X-ray photoelectron spectroscopy (XPS) was carried out on a Thermo Scientific K-Alpha with a monochromatic Al-K_α source. Survey scans were collected over the 0−1400 eV binding energy range with 1 eV resolution and a pass energy of 200 eV. Higher resolution scans (0.1 eV) encompassing the principal peaks of C (1s), O (1s), F (1s), Si (2p), and Ti (2p) were collected at a pass energy of 50 eV; with subsurface layers investigated by Ar-ion sputtering. Chemical environments were deconvolution using CasaXPS software [23], with the binding energies calibrated to graphitic carbon (1s = 285 eV) [24]. UV-visible absorption spectra were measured using a Shimadzu UV-vis 2600 spectrophotometer equipped with an integrating sphere over the wavelength

range 190 – 1400 nm. Film thickness and surface topographies were measured using scanning electron microscopy (SEM) on a JEOL 7000F Field Emission SEM at accelerating voltage of 15 keV. Film morphology was further studied using a Philips CM 200 transmission electron microscope (TEM), after a portion of the film was removed from the substrate using a diamond blade and applied onto a Cu grid and coated with carbon. Surface roughness was measured using a Digital Instruments Dimension 3100 atomic force microscope (AFM) operating in tapping mode with a scan frequency of 2 Hz over a 5 μm × 5 μm area. Results were processed using Gwyddion software [25].

Photoelectrochemical water splitting

All analyses were carried out in a home-made PEEK cell with quartz windows. The electrolyte was 1 M NaOH (Sigma Aldrich, 98 %; pH = 13.6) in Milli-Q-water (Millipore Corp., 18.2 MΩ.cm at 25 °C). A three-electrode configuration was used, with a Pt mesh counter electrode, a Ag/AgCl/saturated-KCl reference electrode (0.197 V_{NHE} at 25 °C; Metrohm) and the TiO_2 photoanode placed at the working electrode. An Autolab potentiostat (PGSTAT12 with an FRA2 module) was used to apply voltage and measure the current extracted from the sample. The applied voltages are reported *vs* the reversible hydrogen electrode (V_{RHE}), converted using the Nernst equation:

$$V_{RHE} = V_{Ag/AgCl} + 0.0591 \times pH + V^{\ominus}_{Ag/AgCl} \quad (2)$$

Current-voltage curves were measured from 0.0 to 2.0 V_{RHE} at a scan rate of 40 $mV.s^{-1}$. A 365 nm LED light was used as the excitation source (LZ1-10U600, LedEngin. Inc.). The

light intensity (~44 mW.cm^{-2}) was measured using an optical power meter (PM 100, Thorlabs) with a power sensor (S120UV, Thorlabs). The incident photon to current efficiency (IPCE) was measured at a fixed potential of 1.23 V_{RHE} (the thermodynamic potential for water oxidation) using an ozone-free xenon lamp (75 W, Hamamatsu) coupled to a monochromator (OBB-2001, Photon Technology International) over the wavelength range 250 – 425 nm. The IPCE was calculated using the following equation:

$$IPCE\ (\%) = \frac{I_{ph} \times 1239.8}{P_{mono} \times \lambda} \times 100 \quad (3)$$

where I_{ph} (mA.cm^{-2}) is the photocurrent, 1239.8 (eV.nm) is a product of Planck's constant with the speed of light, P_{mono} (mW.cm^{-2}) is the power and λ (nm) is the wavelength of the monochromated light. Sample stability was also measured at a fixed potential of 1.23 V_{RHE} under chopped 365 nm LED light for 1 hr.

The solar water splitting activity was simulated from IPCE measurements. This theoretical solar photocurrent (TSP) was determined by multiplying the IPCE with the AM1.5 solar spectrum, and then converting this into a current:

$$TSP\ (mA.cm^{-2}) = \int_{3000\ nm}^{280\ nm} IPCE \times AM1.5\ (photon.cm^{-2}) \times 1000/\ 1C \quad (4)$$

where $1C$ is 6.241 x 10^{18} electrons per second.

RESULTS AND DISCUSSION

Physical characterisation

TiO_2 thin films were grown on FTO glass substrates using a PP-MOCVD process. With the exception of the thinnest film (19 deposition pulses), as-deposited films were brown/black in appearance (92 – 460 pulses). XPS showed that these thicker TiO_2 films contained high levels of carbon (typically between 3– 7 at.% as calculated from XPS depth profile). Ar-ion sputtering was used to etch away surface layers, and the carbon 1s environment was investigated from the surface into the material bulk (**Figure 1a**). Adventitious carbon was observed at the material surface [26]. Ar-ion sputtering removed this adventitious carbon, and revealed a new environment (~281.5 eV) associated with ion induced Ti-C bonding [27]. This type of bonding was observed by Galuska *et al.* on titanium films grown on carbon. Ar-ion sputtering also revealed a carbon environment at ~284.2 eV, that has been attributed to the presence of highly ordered carbon layers [28]. Surface XPS analysis of the Ti 2p environment revealed a binding energy for the Ti $2p_{3/2}$ environment of ~458.7 eV (**Figure S1a**), which corresponds to Ti^{4+} in TiO_2 [29]. No indication of Ti^{3+} formation was observed.

XPS annealing studies here

XRD of the as-deposited samples showed that the thinnest film (19 pulses) was composed of anatase, and that thicker samples contained both anatase and rutile phases of TiO_2 (**Figure S1b**). No diffraction peaks were observed in the XRD pattern of the as-deposited thickest sample (420 pulses); however, after annealing in air, and the subsequent removal of carbon, both anatase and rutile peaks were observed (**Figure 1b**). The anatase: rutile phase fraction was estimated using a refined scale factor, which was determined from the sum total peak counts of each phase (**Equation S1**). Rutile content was low, and ranged

Commented [A1]: Ola, please cite [1] A. Kafizas, X. Wang, S.R. Pendlebury, P.R.F. Barnes, M. Ling, C. Sotelo-Vazquez, R. Quesada-Cabrera, C. Li, I.P. Parkin, J.R. Durrant, Where do Photo-Generated Holes Go in Anatase:Rutile TiO2? A Transient Absorption Spectroscopy Study of Charge Transfer and Lifetime, J. Phys. Chem. A. 120 (2016) 715–723. doi:10.1021/acs.jpca.5b11567.

between 0 – 9 % across all samples (**Table S1**). Interestingly, thicker samples showed higher levels of rutile, where the rutile content increased from 2% in the post-annealed 92 pulse sample to 9% in the post-annealed 460 pulse sample. The XRD of the 184 pulse sample was also measured at various glancing incidence angles (**Figure S3**). The peak height ratio of anatase (101) to rutile (110), at various glancing incidence angles (0.2 to 1.4°), did not vary substantially. Shallow incidence angles primarily probe the surface of the material and steeper incidence angles probe further into the material bulk. Our results showed that the anatase/ rutile phase fraction did not change with material depth.

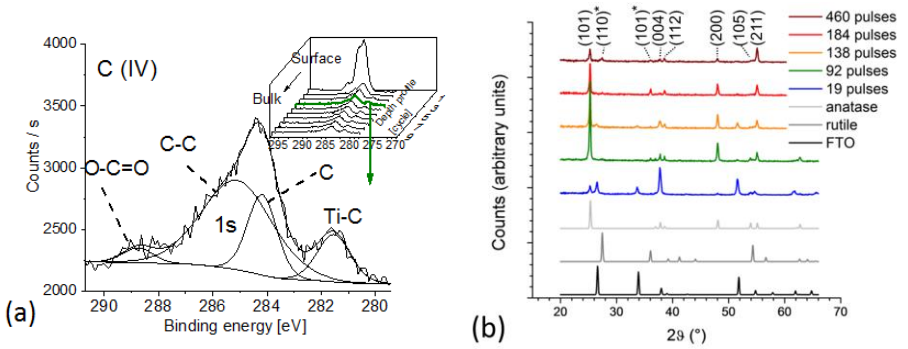

Figure 1: (a) XPS of the carbon 1s binding energy environment in the as-deposited TiO_2 sample made from 184 pulses (inset shows depth profile) and (b) XRD spectra of the air-annealed TiO_2 samples (19 – 460 pulses), alongside anatase, rutile and FTO powder standards. Miller indices correspond to anatase (non-asterisked) and rutile (asterisked) phases.

UV-visible absorption spectroscopy of the post-annealed 19 pulse sample revealed a band edge at ~380 nm (**Figure 2**). There was no significant difference in the UV-visible absorption spectrum of the 19 pulse sample before and after annealing, which we attribute to the lack of carbon incorporated into these films. A Tauc plot showed that the bandgap of the

19 pulse sample was ~3.1 eV (**Figure S4**), similar to literature values for anatase TiO_2 (~3.2 eV) [30, 31]. UV-visible absorption spectroscopy of the as-deposited 92 pulse sample revealed a red-shifted band edge at ~410 nm, alongside strong absorption into the visible (**Figure 2**). The strong absorption in the visible was due to a high concentration of carbon presence in this material. This was typical of thicker samples made from a higher number of deposition pulses, which all appeared brown/ black in colour. However, after annealing in air, the 92 pulse sample maintained its red-shifted band edge and showed a decrease in absorption in the visible. This decrease in visible light absorption was attributed to the removal of carbon by annealing, resulting in a colour change to hazy white (**Figure 2**, inset). After annealing, the 92 pulse sample possessed a higher degree of visible light "absorption" compared with the thinner 19 pulse sample. Primarily, this was not due to light absorption, but rather, an increase in the diffuse scattering of light (which gave rise to a false positive of visible light absorption). This was caused by an increase in surface roughness in thicker films, and the resulting formation of surface nanostructures, as evidenced by SEM (**Figure 3**).

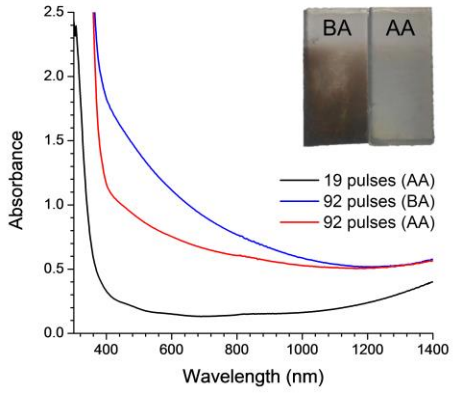

Figure 2: UV-visible absorption spectroscopy of the 19 pulse sample after annealing (AA), and the 92 pulse sample before annealing (BA) and after annealing (inset shows a photograph of the 92 pulse sample before and after annealing).

SEM was used to investigate the topography and thickness of the samples (**Figure 3**). Film thickness increased from ~100 nm in the 19 pulse sample to ~11 μm in the 460 pulse sample. This increase in film thickness was not linear with the number of deposition pulses; with the growth rate increasing exponentially with the number of pulses (~5, ~6, ~14 and ~23 nm per pulse for the 19, 92, 184 and 460 pulse samples respectively). The 19 pulse sample consisted of randomly organised crystallites. The 92 pulse sample consisted of nanostructured protruding rounded structures. The thicker films (184 and 460 pulses) consist of nanostructured dendrites with larger diameters in thicker films. The surfaces of the dendrites present at a jagged array of highly ordered sheets. No substantial change in microstructure or film thickness was observed after annealing the samples in air (**Figure S5**).

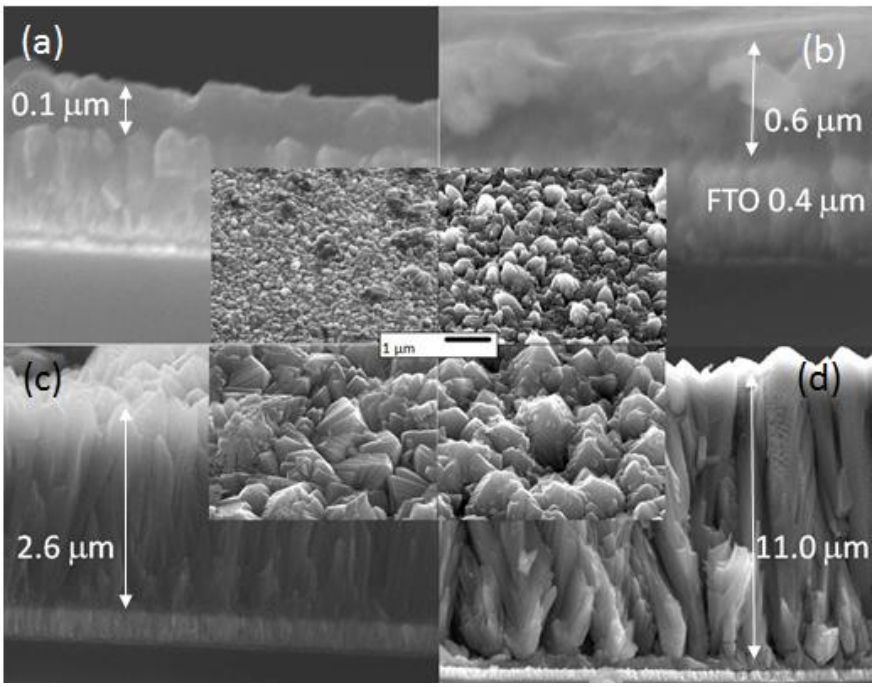

Figure 3: Side-on cross-sectional SEM images of TiO_2 samples, after annealing in air, made from (a) 19, (b) 92, (c) 184 and (d) 460 pulses (inserts in the centre show top-down images of surface topography). Arrows indicate mean film thickness given.

AFM was also used to investigate the surface topography of all samples (**Figure S6**). Both surface area and surface roughness increased with film thickness (**Table 1**). The surface area, per geometric 25 μm^2, increased from 36.0 μm^2 in the 19 pulse sample to 56.3 μm^2 in the 460 pulse sample and the root mean square (RMS) roughness increased from 42.3 nm in the 19 pulse sample to 257 nm in the 460 pulse sample. No significant change in surface area or surface roughness was observed after annealing in air (**Figure S7**).

TiO_2 microstructure

Fragments scraped from the 184 pulse sample contained crystallite fragments that could be imaged by TEM, which showed that these fragments were primarily composed of anatase dendrites (**Figure 4**). The approximate length and width of each dendrite arm was 70 nm and 10-20 nm, respectively. High resolution imaging reveals lattice fringes and the spacing corresponds to (101) anatase planes. These (101) anatase planes were perpendicular to the dendrite fragment lying flat on the TEM grid, but the plane of the fragment could not be identified here. Fringes corresponding to rutile crystals, observed by XRD, were not observed by TEM analysis. No carbon structures were found in the TEM analysis suggesting that carbon forms thin layers at crystallite interfaces only, which can also account for lack of structural changes in the film before and after annealing as seen in **Figure S5** and **Figure S7**.

Dendritic films of anatase TiO_2 have been grown using a number of synthesis routes and various explanations have been given for their formation, focusing mostly on deposition conditions [32-35]. Takahashi *et. al.* reported both anatase and mixed phase anatase/rutile TiO_2 films deposited at 500 ˚C using TTIP [34]. Only anatase growth was observed at low carrier gas flows (N_2, 0.2 cm^3s^{-1}), whereas rutile content increased exponentially with an increase in flow rate. Similar nanostructures were observed by Takahashi *et. al.*, to the dendrites observed herein, however no TEM analysis was presented and nanoscale features were not described [34]. Biswas *et. al.* showed that nanoscale anatase columns with (112) texture and widths of approximately 20 – 30 nm could be grown by aerosol-assisted CVD at 500 ˚C [18, 36, 37]. Goossens *et al*. [33] reported nanostructured dendritic anatase films, with a similar morphology to Takahashi *et. al.*'s [34], deposited using APCVD from mixtures of TTIP and $TiCl_4$ in the temperature range of 300 – 350 ˚C. The water splitting activity of

dendritic titania, grown using the aforementioned CVD processes, have not previously been examined.

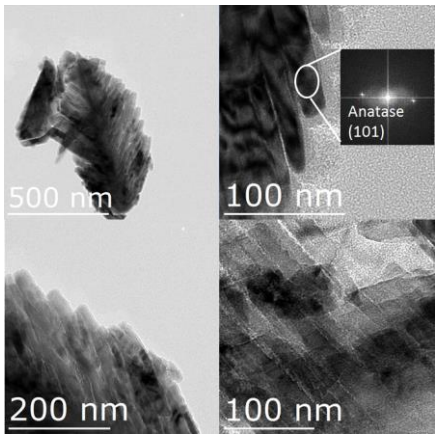

Figure 4: TEM micrographs of the as-deposited TiO_2 sample grown from 184 pulses. Measurement of the d-spacing (top right) showed that these crystals were anatase TiO_2 single crystals.

Photoelectrochemical water splitting

The photoelectrochemical water splitting activity of our TiO_2 photoelectrodes was examined, both before and after being annealed in air. Current voltage curves were measured in 1 M NaOH (pH = 13.6), sweeping the voltage from 0.0 to 2.0 V_{RHE}. A 365 nm LED (~44 $mW.cm^{-2}$) was turned on and off, roughly every second. The current-voltage curves, measured under front irradiation, are shown in **Figure 5** for a series of samples made from a range of deposition pulses. We will first discuss the performance of as-deposited samples, before they were annealed in air. The 19 pulse sample, which possessed the least nanostructure and consisted solely of the anatase phase, showed the earliest photocurrent onset (~0.1 V_{RHE}) and

plateau (~0.8 V_{RHE}), and showed a photocurrent of ~1.4 mA.cm^{-2} at 1.23 V_{RHE}. The 92 pulse sample, which possessed dendritic nanostructure and was composed of a mixture of anatase and rutile phases, showed a similarly early photocurrent onset but plateaued later (~1.3 V_{RHE}). The 92 pulse sample showed a photocurrent of ~2.4 mA.cm^{-2} at 1.23 V_{RHE}. A decrease in photoelectrochemical performance was observed in thicker materials, the 184 and 460 pulse samples showing photocurrents of ~1.4 mA.cm^{-2} and ~0.1 mA.cm^{-2} at 1.23 V_{RHE} respectively. We will now discuss the performance of samples after being annealed in air. The 19 pulse sample showed no significant change to its performance before being annealed. However, the 92 pulse sample showed substantial improvements in performance, where the photocurrent onset shifted cathodically to ~0.1 V_{RHE}, the photocurrent plateaued earlier (~1.0 V_{RHE}) and the photocurrent increased substantially; reaching ~4.6 mA.cm^{-2} at 1.23 V_{RHE}. Similar enhancements in photoelectrochemical water splitting activity were observed in the 184 and 460 pulse samples; reaching ~3.5 mA.cm^{-2} and ~3.9 mA.cm^{-2} at 1.23 V_{RHE} respectively. Turning our attention to the photoelectrochemical performance when irradiated from the back (**Figure S8**), we find similar trends to what was observed under front irradiation, both before and after being annealed in air, with the exception that the thickest sample (460 pulses) showed the highest activity.

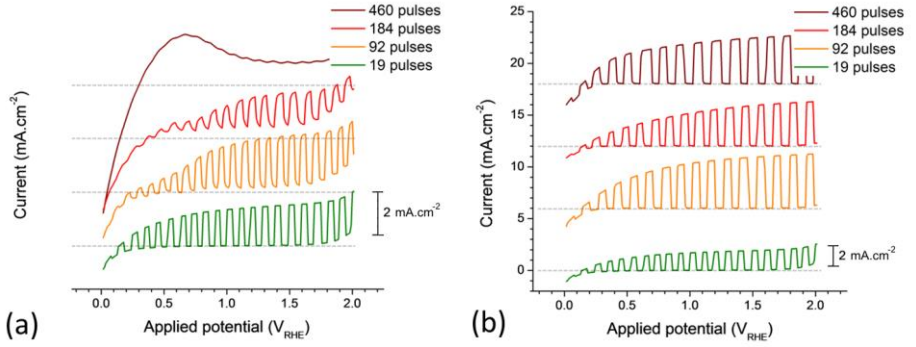

Figure 5: Current-voltage curves for a series of TiO_2 samples measured under front irradiation (a) before and (b) after being annealed in air. Samples were measured in 1 M NaOH (pH = 13.6), the current was swept from 0.0 to 2.0 V_{RHE} at a scan rate of 40 $mV.s^{-1}$ and a 365 nm LED (~44 $mW.cm^{-2}$) was turned on and off roughly every second. Dotted grey lines represent the zero-line of current flow for each sample (*i.e.* 0 $mA.cm^{-2}$).

IPCEs were measured under front irradiation at a constant applied potential of 1.23 V_{RHE}, both before and after being annealed in air (**Figure 6**). Before annealing, there was a clear trend in activity, where the thinnest sample (19 pulses) showed higher light conversion efficiencies, and increases in film thickness resulted in lower efficiencies. Intriguingly, all samples showed a sharp cut-off in activity above 375 nm, despite thicker samples containing a significant rutile component (E_{bg} ~3.0 eV, ~ 410 nm) and a more red-shifted band edge (**Figure 2**). This indicated that only the anatase component was active in splitting water for non-annealed films (E_{bg} ~3.2 eV, ~ 388 nm). Post-annealing, the 92 pulse sample showed a dramatic increase in activity, matching the light conversion efficiencies of the 19 pulse sample in the UV-region (250 – 300 nm), and also showing extended activity into the visible. Post-annealing, thicker samples, which contained a rutile component, showed higher visible light activities than the thinnest sample (19 pulses), which solely contained anatase. When irradiating the samples from the back (*i.e.* through the FTO layer), a loss in UV activity from

250 – 325 nm was observed (**Figure S9**). This was attributed to UV absorption by the FTO layer, which blocked UV light from reaching the TiO_2 layer. Similar trends in light conversion behaviour were observed, pre and post-annealing, to those found under front irradiation; with the exception that the thickest sample (460 pulses) showed the highest levels of activity. Of note, the TiO_2 photoelectrodes grown herein were durable, and showed no change in photocurrent over a period of testing for one hour (**Figure S10**).

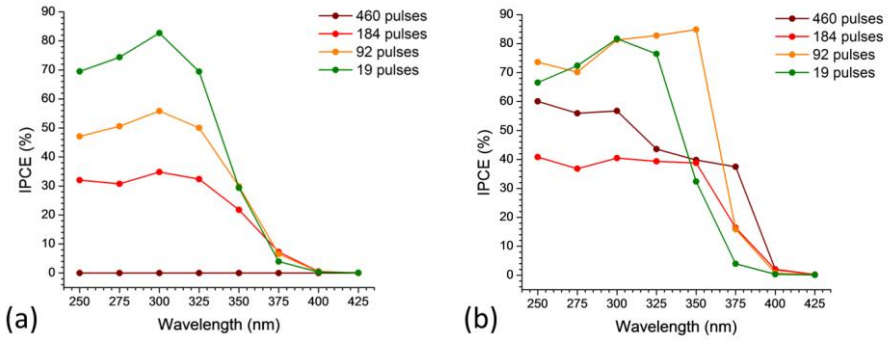

Figure 6: IPCE measured at a constant applied potential of 1.23 V_{RHE} in 1 M NaOH (pH = 13.6) for a series of TiO_2 samples under front irradiation (a) before and (b) after annealing.

Looking at general trends in photoelectrochemical activity, thinner samples were more active than thicker samples before being annealed. However, after annealing, thicker samples showed substantial increases in activity; both under 365 nm irradiation (**Figure 5**) and into the visible (**Figure 6**). This was attributed to two complimentary physical properties: (i) an increased nanostructure and (ii) the activation of the rutile component. We will discuss each point in turn.

An increase in nanostructure is often beneficial for photoelectrochemical water splitting systems, and is attributed to the enhancement of light absorption near the semiconductor/ electrolyte interface (as opposed to the bulk). This is of particular importance in TiO_2, where the hole diffusion length is on the order of 10's of nanometres [14]. On the other hand, given the long diffusion length of electrons in TiO_2, on the order of several micrometers [38], electron extraction into the FTO layer is possible so long as film thickness does not surpass this diffusion limit. Of note, this electron diffusion limit was likely surpassed by our thickest sample (460 pulses, ~11 μm), and as a consequence, showed higher light conversion efficiencies under back irradiation (**Figure S9**) than front irradiation (**Figure 6**). Thicker, and more nanostructured photoelectrodes, often show higher levels of activity than thinner, and more flat-structured photoelectrodes, as they better utilise light that is absorbed deeper into the material (*i.e.* wavelengths at the band edge, that are not absorbed as strongly as wavelengths lower than the band edge). In addition to this, nanostructured materials scatter light more effectively than flatter structures, and have been used to good effect in enhancing the performance of photovoltaic devices [39, 40].

Rutile was found more prominently in thicker samples (92 – 460 pulse depositions), and upon annealing, the water splitting activity was extended into the near-visible (**Figure 6**). This was due to the "activation" of the rutile component upon annealing. It was not that annealing resulted in an increase in rutile formation in our materials (as evidenced by our XRD studies, see **Table S1**), but rather, it was the removal of carbon through annealing that resulted in the activation of rutile already present in our materials (**Figure S**2). This was because carbon was an inhibitor, which prevented electron extraction from our materials, and inhibited the performance of rutile more so than anatase. In the 92 pulse sample, annealing

resulted in a synergic interaction between the anatase and rutile phases, matching the UV light conversion efficiencies of the 19 pulse sample (*i.e.* pure anatase) and showing extended activity into the visible. Synergic interactions in anatase: rutile composites are frequently observed, where in fact, P25 Degussa TiO_2, a commercially available powder composite composed of both anatase and rutile phases, is often considered the benchmark photocatalyst given its high activity for a range of photocatalytic process; including water splitting) [41]. The physical properties and water splitting activities of our TiO_2 photoelectrodes, after being annealed in air, is shown in **Table 1.**

Table 1: Summary of the physical properties and water splitting performance of our TiO_2 photoelectrodes, after being annealed in air.

Sample (number of pulses)	**Surface area per geometric 25 μm² (μm²)**	**RMS roughness (nm)**	**Film thickness (μm)**	**Photocurrent (mA.cm^{-2}) – 365 nm light (~44 mW.cm^{-2})***	**IPCE at 350 nm (%)***
19	36.0	42.3	0.1	1.4	32
92	32.6	97.1	0.6	4.6	85
182	41.1	123	2.6	3.5	39
460	56.3	257	11.0	3.9	40

*when held at 1.23 V_{RHE} and irradiated from the front (semiconductor-electrolyte interface).

We will now turn our attention to the role of carbon in relation to the water splitting activity of our TiO_2 photoelectrodes. As-deposited samples, grown from 92 – 460 deposition pulses, possessed high levels of carbon (typically between 3 – 7 at.%). Carbon has a work function of ~4.8 eV [42], and would thus possess a Fermi level of ~0.3 V_{RHE}. As the conduction band potentials of anatase and rutile are more negative than this Fermi level [41]. there is a thermodynamic driving force for photo-generated electrons to move into carbon sites. Our XPS and TEM analyses indicated carbon grew mostly in sheets, located between

dendritic anatase crystals. As such, there is likely no consistent or inter-connected carbon structure that runs through the TiO_2 structure. This means that photo-generated electrons, which move into carbon sites, are likely trapped within these isolated carbon sheets; increasing the likelihood of electron-hole recombination (**Figure 7**a). This was evidenced in our current-voltage curves, where dark current capacitance was observed; increasingly so in thicker films. Moreover, thicker films showed lower photocatalytic activities under front irradiation than thinner films (**Figure 5**b), in addition to a slower rise in photocurrent when the light was turned on, which we attribute to slower electron extraction kinetics due to the inhibiting role of carbon. However, after annealing the samples in air at 500 °C, carbon was oxidised and removed, resulting in substantially higher water splitting activity (**Figure 5** and **Figure 6**). Although carbon inhibits water splitting in our TiO_2 photoelectrodes, our physical characterisations indicate carbon templates the growth of dendritic TiO_2 nanostructures; essential for enhancing the water splitting activity of TiO_2-based photoelectrodes [43, 44]. This, coupled with the fact that carbon can be easily removed by annealing, shows that it may serve as a tool for creating nanostructured water splitting devices.

Commented [A2]: Remove reference 43, as requested by the referee.

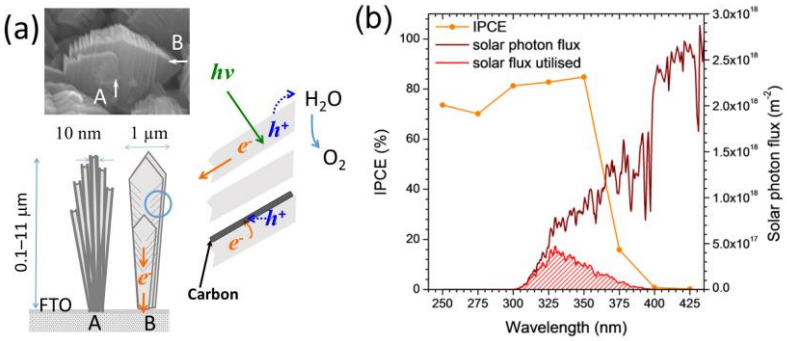

Figure 7: (a) A cartoon that describes how sheets of carbon form between TiO_2 crystals, and how the material functions in photocatalytically splitting water under a positive applied potential and ultra-bandgap light. (b) The theoretical solar photocurrent determined for the 92 pulse sample under front irradiation.

Theoretical solar photocurrent (TSP) was determined by multiplying IPCE spectra with the AM 1.5 solar spectrum (Equation 4). Our most active sample under front irradiation (92 pulses) showed a TSP of ~1.2 $mA.cm^{-2}$ at 1.23 V_{RHE} under 1 sun irradiance (**Figure 7**b), and is compared with TiO_2-based photoelectrodes from the literature (**Table 2**). Wijayantha *et. al.* grew cauliflower-structured anatase TiO_2 photoelectrodes using an aerosol-assisted CVD route [45]. These photoelectrodes showed photocurrents of ~0.2 $mA.cm^{-2}$ at 1.23 V_{RHE} under 1 sun irradiance (100 $mW.cm^{-2}$, Xe lamp). Zheng *et al.*, using hydrothermal methods, grew hierarchically branched single crystal rutile nanorods [35]. These photoelectrodes showed light conversion efficiencies near 70 % at 380 nm and photocurrents of ~0.83 $mA.cm^{-2}$ at 0.8 V_{RHE} under near 1 sun irradiance (88 $mW.cm^{-2}$, Xe lamp). Gu *et. al.* grew nanostructured TiO_2 photoelectrodes using a two-step hydrothermal method, in which highly oriented rutile nanorods were grown and decorated with anatase branches [44]. These photoelectrodes showed light conversion efficiencies above 60 % in the UV region, and photocurrents of ~1.0 $mA.cm^{-2}$ at 0.8 V_{RHE} under 1 sun irradiance (100 $mW.cm^{-2}$, Xe lamp). Comparing the literature, the photoelectrodes synthesised herein using CVD show similar water splitting activities to some of the leading TiO_2-based materials. Given CVD is an economically viable and upscalable process, which is currently used to grow self-cleaning TiO_2 coatings on mass scale (*e.g.* Pilkington NSG Activ), this article should serve as a model example for upscalably growing nanostructured photoelectrodes made from visible-light active materials that can harness a greater portion of sunlight.

Table 2: Summary of the phases, structures, synthesis routes and water splitting performances of example TiO_2-based photoelectrodes in the literature, as compared with our best performing material (the 92 pulse sample, post annealing in air).

Synthetic route	Phase	Architecture	IPCE at 350 nm (%)*	Photocurrent ($mA.cm^{-2}$) at 1 sun irradiance*	reference
PP-MOCVD	anatase: rutile	dendritic	85	~1.2	herein
Aerosol-assisted CVD	anatase	cauliflower-structured	n/a	~0.2	[45]
Hydrothermal	rutile	branched nanorods	~32	~0.85	[35]
Hydrothermal	anatase: rutile	rutile nanorods; anatase branches	~57	~1.1	[44]

*when held at 1.23 V_{RHE} and irradiated from the front (semiconductor-electrolyte interface).

CONCLUSIONS

The photoelectrochemical water oxidation performance of nanostructured anatase, and anatase-rutile TiO_2 photoelectrodes was investigated; as well as the role of co-deposited carbon. Highly nanostructured architectures were produced by an upscalable CVD route (PP-MOCVD), where the deposition parameters could be varied to fine-tune several material properties such as: (i) film thickness, (ii) the anatase-rutile phase fraction, and (iii) topography.

Photoelectrodes that contained both the anatase and rutile phases showed synergistic enhancements in activity, compared with anatase alone, with incident photon-to-current efficiencies above 80 % in the UV region, and photocurrents of ~1.2 $mA.cm^{-2}$ at 1.23 V_{RHE}. We propose that co-deposited carbon might play a role in templating the growth of dendritic nanostructures. Although carbon inhibited water splitting in this system, it could be removed by a post-deposition annealing process, resulting in highly active and nanostructured photoelectrodes. We believe that this article should serve as a model example for the

upscalable growth of highly active nanostructured photoelectrodes, where similar design principles should be applied to more visible-light materials to realise enhanced solar activity.

ACKNOWLEDMENTS

This work is supported by New Zealand Ministry for Business, Innovation and Employment under the High Value Manufacturing Science and Technology Research Program Contract No. CONT-42986-HVMSTR-UOC (UOCX1501) and a research contract from KOTI Technologies Limited. I.P.P. thanks the Engineering and Physical Sciences Research Council (EPSRC) for their financial support (EP/L015862/1). A.K. thanks Imperial College for a Junior Research Fellowship.

REFERENCES

[1] W.S. Broecker, Climatic Change: Are We on the Brink of a Pronounced Global Warming?, Science, 189 (1975) 460-463.
[2] N. Gruber, Warming up, turning sour, losing breath: ocean biogeochemistry under global change, Philosophical Transactions of the Royal Society of London A: Mathematical, Physical and Engineering Sciences, 369 (2011) 1980-1996.
[3] B.K. Sovacool, The intermittency of wind, solar, and renewable electricity generators: Technical barrier or rhetorical excuse?, Utilities Policy, 17 (2009) 288-296.
[4] A. Fujishima, K. Honda, Photolysis-decomposition of water at the surface of an irradiated semiconductor, Nature, 238 (1972) 37-38.
[5] F.E. Osterloh, Inorganic materials as catalysts for photochemical splitting of water, Chem. Mater, 20 (2008) 35-54.
[6] F.E. Osterloh, Inorganic nanostructures for photoelectrochemical and photocatalytic water splitting, Chemical Society Reviews, 42 (2013) 2294-2320.
[7] A.L. Linsebigler, G. Lu, J.T. Yates Jr, Photocatalysis on TiO_2 surfaces: principles, mechanisms, and selected results, Chemical reviews, 95 (1995) 735-758.
[8] A. Fujishima, T.N. Rao, D.A. Tryk, Titanium dioxide photocatalysis, Journal of Photochemistry and Photobiology C: Photochemistry Reviews, 1 (2000) 1-21.

[9] Y. Li, Y.-L. Li, B. Sa, R. Ahuja, Review of two-dimensional materials for photocatalytic water splitting from a theoretical perspective, Catalysis Science & Technology, 7 (2017) 545-559.
[10] J.R. Bolton, S.J. Strickler, J.S. Connolly, Limiting and realizable efficiencies of solar photolysis of water, Nature, 316 (1985) 495-500.
[11] A. Kafizas, Y. Ma, E. Pastor, S.R. Pendlebury, C. Mesa, L. Francàs, F. Le Formal, N. Noor, M. Ling, C. Sotelo-Vazquez, The water oxidation kinetics of accumulated holes on the surface of a TiO_2 photoanode: A rate law analysis, ACS Catalysis, (2017).
[12] S.J. Moniz, S.A. Shevlin, D.J. Martin, Z.-X. Guo, J. Tang, Visible-light driven heterojunction photocatalysts for water splitting–a critical review, Energy & Environmental Science, 8 (2015) 731-759.
[13] A. Kafizas, R. Godin, J.R. Durrant, Charge Carrier Dynamics in Metal Oxide Photoelectrodes for Water Oxidation, Semiconductors and Semimetals, (2017).
[14] P. Salvador, Hole diffusion length in n-TiO_2 single crystals and sintered electrodes: Photoelectrochemical determination and comparative analysis, Journal of Applied Physics, 55 (1984) 2977-2985.
[15] A. Kay, I. Cesar, M. Grätzel, New benchmark for water photooxidation by nanostructured α-Fe_2O_3 films, Journal of the American Chemical Society, 128 (2006) 15714-15721.
[16] J. Luo, L. Steier, M.-K. Son, M. Schreier, M.T. Mayer, M. Grätzel, Cu_2O nanowire photocathodes for efficient and durable solar water splitting, Nano letters, 16 (2016) 1848-1857.
[17] A. Kafizas, L. Francàs, C. Sotelo-Vazquez, M. Ling, Y. Li, E. Glover, L. McCafferty, C. Blackman, J. Darr, I. Parkin, Optimizing the Activity of Nanoneedle Structured WO_3 Photoanodes for Solar Water Splitting: Direct Synthesis via Chemical Vapor Deposition, The Journal of Physical Chemistry C, 121 (2017) 5983-5993.
[18] W.-J. An, W.-N. Wang, B. Ramalingam, S. Mukherjee, B. Daubayev, S. Gangopadhyay, P. Biswas, Enhanced water photolysis with Pt metal nanoparticles on single crystal TiO_2 surfaces, Langmuir, 28 (2012) 7528-7534.
[19] K. Choy, Chemical vapour deposition of coatings, Progress in materials science, 48 (2003) 57-170.
[20] A. Kafizas, I. Parkin, Materials for a sustainable future, Chapter 20 - Glass and New Technologies, 1st Edition, Royal Society of Chemistry2012, Cambridge.
[21] V. Siriwongrungson, S.P. Krumdieck, M.M. Alkaisi, Conformality Investigation of Titanium Dioxide Thin Films on 3D Micrometer and Nanometer scale Features by Pulsed Pressure Metal organic CVD, Chemical Vapor Deposition, 17 (2011) 327-336.
[22] D. Lee, S. Krumdieck, S.D. Talwar, Scale-up design for industrial development of a PP-MOCVD coating system, Surface and Coatings Technology, 230 (2013) 39-45.
[23] J. Walton, P. Wincott, N. Fairley, A. Carrick, Peak Fitting with CasaXPS: A Casa Pocket Book, (2010).
[24] P. Swift, Adventitious carbon—the panacea for energy referencing?, Surface and Interface Analysis, 4 (1982) 47-51.
[25] D. Nečas, P. Klapetek, Gwyddion: an open-source software for SPM data analysis, Open Physics, 10 (2012) 181-188.

[26] M.C. Biesinger, L.W. Lau, A.R. Gerson, R.S.C. Smart, Resolving surface chemical states in XPS analysis of first row transition metals, oxides and hydroxides: Sc, Ti, V, Cu and Zn, Applied Surface Science, 257 (2010) 887-898.
[27] A. Galuska, J. Uht, N. Marquez, Reactive and nonreactive ion mixing of Ti films on carbon substrates, Journal of Vacuum Science & Technology A: Vacuum, Surfaces, and Films, 6 (1988) 110-122.
[28] J. Morar, F. Himpsel, G. Hollinger, J. Jordan, G. Hughes, F. McFeely, C 1s excitation studies of diamond (111). I. Surface core levels, Physical Review B, 33 (1986) 1340.
[29] A. Burke, C. Brown, W. Bowling, J. Glaub, D. Kapsch, C. Love, R. Whitaker, W. Moddeman, Ignition mechanism of the titanium–boron pyrotechnic mixture, Surface and Interface Analysis, 11 (1988) 353-358.
[30] H.T. Grahn, Introduction to semiconductor physics, World Scientific Publishing Co Inc1999.
[31] K.M. Reddy, S.V. Manorama, A.R. Reddy, Bandgap studies on anatase titanium dioxide nanoparticles, Materials Chemistry and Physics, 78 (2003) 239-245.
[32] A. Ito, S. Nishigaki, T. Goto, A feather-like structure of β-Al_2TiO_5 film prepared by laser chemical vapor deposition, Journal of the European Ceramic Society, 35 (2015) 2195-2199.
[33] A. Goossens, E.L. Maloney, J. Schoonman, Gas-Phase Synthesis of Nanostructured Anatase TiO_2, Chemical Vapor Deposition, 4 (1998) 109-114.
[34] Y. Takahashi, H. Suzuki, M. Nasu, Rutile growth at the surface of TiO_2 films deposited by vapour-phase decomposition of isopropyl titanate, Journal of the Chemical Society, Faraday Transactions 1: Physical Chemistry in Condensed Phases, 81 (1985) 3117-3125.
[35] I.S. Cho, Z. Chen, A.J. Forman, D.R. Kim, P.M. Rao, T.F. Jaramillo, X. Zheng, Branched TiO_2 nanorods for photoelectrochemical hydrogen production, Nano Letters, 11 (2011) 4978-4984.
[36] W.-J. An, E. Thimsen, P. Biswas, Aerosol-chemical vapor deposition method for synthesis of nanostructured metal oxide thin films with controlled morphology, The Journal of Physical Chemistry Letters, 1 (2009) 249-253.
[37] W.-N. Wang, W.-J. An, B. Ramalingam, S. Mukherjee, D.M. Niedzwiedzki, S. Gangopadhyay, P. Biswas, Size and structure matter: enhanced CO_2 photoreduction efficiency by size-resolved ultrafine Pt nanoparticles on TiO_2 single crystals, Journal of the American Chemical Society, 134 (2012) 11276-11281.
[38] W. Leng, P.R. Barnes, M. Juozapavicius, B.C. O'Regan, J.R. Durrant, Electron diffusion length in mesoporous nanocrystalline TiO_2 photoelectrodes during water oxidation, The Journal of Physical Chemistry Letters, 1 (2010) 967-972.
[39] W. Zhou, X. Liu, J. Cui, D. Liu, J. Li, H. Jiang, J. Wang, H. Liu, Control synthesis of rutile TiO_2 microspheres, nanoflowers, nanotrees and nanobelts via acid-hydrothermal method and their optical properties, CrystEngComm, 13 (2011) 4557-4563.
[40] R. Yang, Y.-L. Chueh, J.R. Morber, R. Snyder, L.-J. Chou, Z.L. Wang, Single-crystalline branched zinc phosphide nanostructures: synthesis, properties, and optoelectronic devices, Nano letters, 7 (2007) 269-275.
[41] A. Kafizas, X. Wang, S.R. Pendlebury, P. Barnes, M. Ling, C. Sotelo-Vazquez, R. Quesada-Cabrera, C. Li, I.P. Parkin, J.R. Durrant, Where Do Photogenerated Holes Go in Anatase: Rutile TiO_2? A Transient Absorption Spectroscopy Study of Charge Transfer and Lifetime, The Journal of Physical Chemistry A, 120 (2016) 715-723.

[42] D. Cao, G.-Q. Lu, A. Wieckowski, S.A. Wasileski, M. Neurock, Mechanisms of methanol decomposition on platinum: A combined experimental and ab initio approach, The Journal of Physical Chemistry B, 109 (2005) 11622-11633.
[43] J.-S. Yang, W.-P. Liao, J.-J. Wu, Morphology and interfacial energetics controls for hierarchical anatase/rutile TiO_2 nanostructured array for efficient photoelectrochemical water splitting, ACS applied materials & interfaces, 5 (2013) 7425-7431.
[44] J. Liu, X. Yu, Q. Liu, R. Liu, X. Shang, S. Zhang, W. Li, W. Zheng, G. Zhang, H. Cao, Surface-phase junctions of branched TiO_2 nanorod arrays for efficient photoelectrochemical water splitting, Applied Catalysis B: Environmental, 158 (2014) 296-300.
[45] A.A. Tahir, T. Peiris, K. Wijayantha, Enhancement of photoelectrochemical performance of AACVD-produced TiO_2 electrodes by microwave irradiation while preserving the nanostructure, Chemical Vapor Deposition, 18 (2012) 107-111.
[46] G. Wang, H. Wang, Y. Ling, Y. Tang, X. Yang, R.C. Fitzmorris, C. Wang, J.Z. Zhang, Y. Li, Hydrogen-treated TiO_2 nanowire arrays for photoelectrochemical water splitting, Nano letters, 11 (2011) 3026-3033.

Commented [A3]: Ola, please make sure that all reference to articles 43 and 46 are removed from the manuscript.

SUPPORTING INFORMATION

High efficiency water splitting photoanodes composed of nano-structured anatase-rutile TiO_2 heterojunctions by pulsed-pressure MOCVD

Aleksandra J. Gardecka,[a] Catherine Bishop,[a] Darryl Lee,[a] Sacha Corby,[d] Ivan P. Parkin,[b] Andreas Kafizas[c]* and Susan Krumdieck[a]*

[a]Department of Mechanical Engineering, University of Canterbury, Christchurch, 8041, New Zealand

[b]Materials Chemistry Centre, Department of Chemistry, University College London, 20 Gordon Street, London, WC1H 0AJ, UK

[c]Department of Chemistry, Imperial College London, South Kensington, London, SW7 2AZ, UK

*corresponding authors: a.kafizas@imperial.ac.uk, susan.krumdieck@canterbury.ac.nz

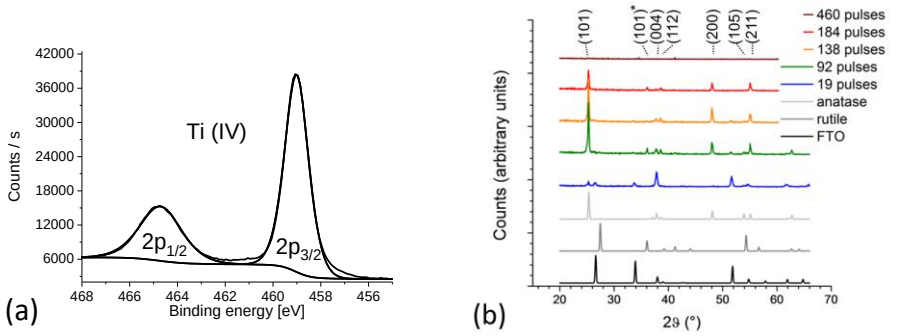

Figure S1: (a) XPS of the surface Ti 2p binding energy environment in the as-deposited TiO_2 sample made from 184 pulses and (b) XRD patterns of the as-deposited TiO_2 samples (19 – 460 pulses), alongside anatase, rutile and FTO powder standards. Miller indices correspond to anatase (non-asterisked) and rutile (asterisked) phases.

Figure S2: XPS annealing study goes here

As all samples showed some degree of preferred growth, a refined scale factor was estimated by taking the sum total counts of each modelled phase, allowing us to estimate phase fraction:

$$anatase\ (wt.\%) = \left[\frac{S_a \rho_a V_r^2}{S_a \rho_a V_r^2 + S_r \rho_r V_r^2}\right] \times 100$$

(Equation S1)

where S is the refined scale factor, ρ is the density, V is the unit cell volume and subscript labels a and r refer to the anatase and rutile phases respectively.

Table S1: Summary of the anatase: rutile (%) phase fraction in of our TiO_2 photoelectrodes, determined using XRD for samples both before and after annealing in air.

Sample (number of pulses)	**Before annealing**	**After annealing**
	anatase: rutile (%)	**anatase: rutile (%)**
19	100: 0	100: 0
92	94: 6	98: 2
138	97: 3	95: 5
182	95: 5	94: 6
460	n/a*	91: 9

*Material was too amorphous to determined phase fraction

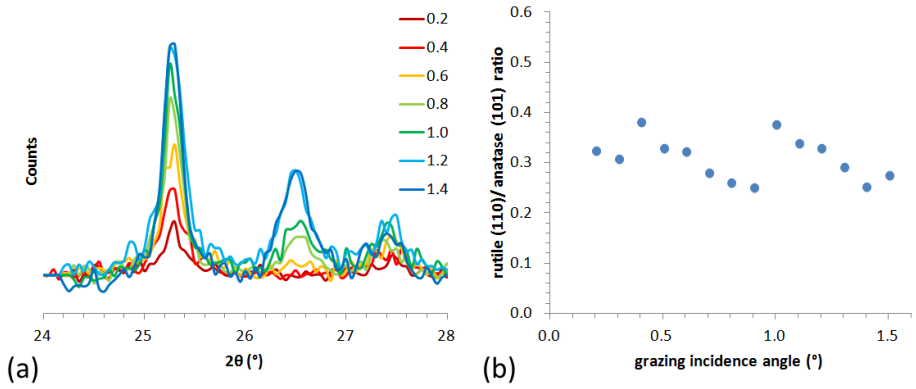

Figure S3: XRD of the 184 pulse sample, after being annealed, measured at various glancing incidence angles (0.2 – 1.4°) over the range 24° < 2θ < 28°. Peaks were observed at 25.5, 26.5 and 27.5° and corresponded to anatase (101), FTO (110) and rutile (110) respectively.

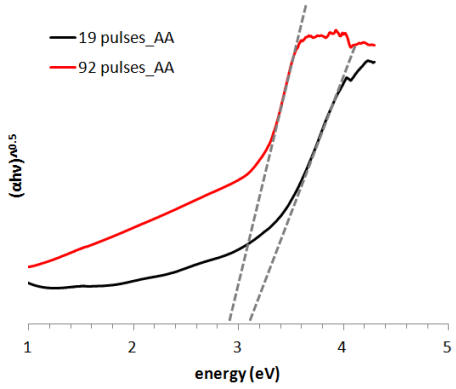

Figure S4: Tauc plot of the (absorption coefficient x Planck's constant x frequency)$^{1/2}$ *vs* the light energy (eV) for the 19 and 92 pulse samples after being annealed in air, revealing bandgap energies of ~3.1 and 2.9 eV respectively.

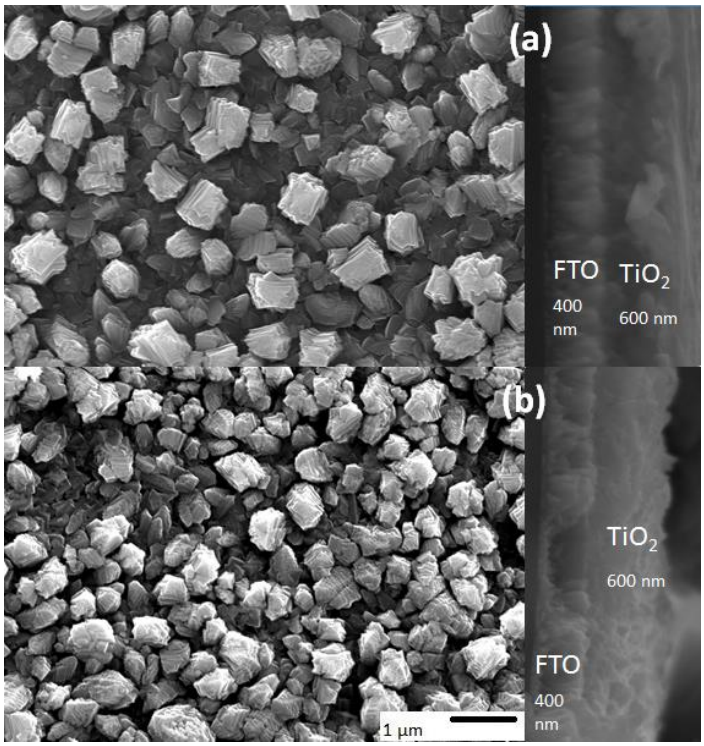

Figure S5: SEM micrographs of the 92 pulse TiO_2 sample (a) as-deposited and (b) after being annealed in air.

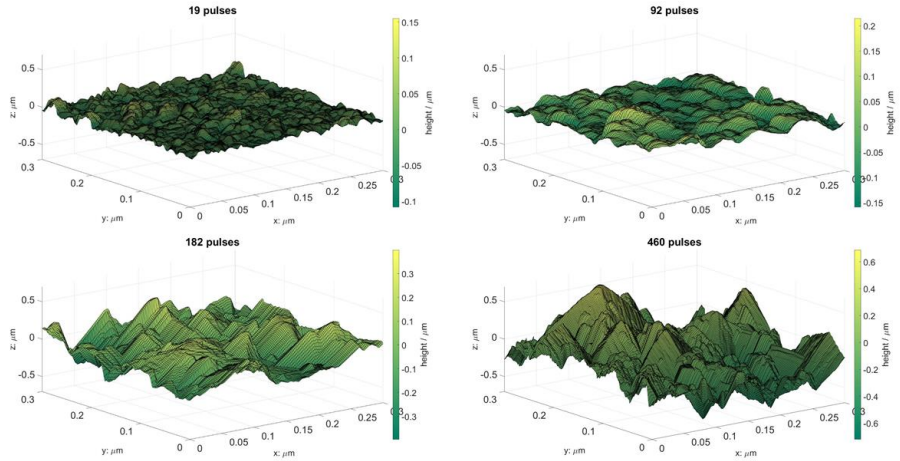

Figure S6: Surface topography, measured by AFM, for all samples after being annealed in air.

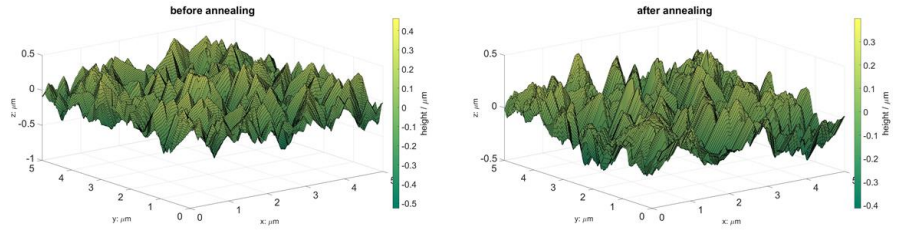

Figure S7: Surface topography, measured by AFM, for the 92 pulse sample before and after being annealed in air.

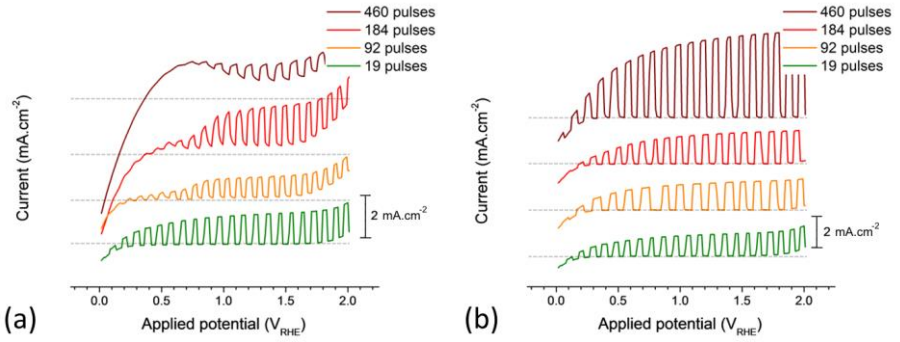

Figure S8: Current-voltage curves for a series of TiO_2 samples measured under back irradiation (a) before and (b) after being annealed in air. Samples were measured in 1 M NaOH (pH = 13.6), the current was swept from 0.0 to 2.0 V_{RHE} at a scan rate of 40 $mV.s^{-1}$ and a 365 nm LED (~44 $mW.cm^{-2}$) was turned on and off roughly every second. Dotted grey lines represent the zero-line of current flow for each sample (*i.e.* 0 $mA.cm^{-2}$).

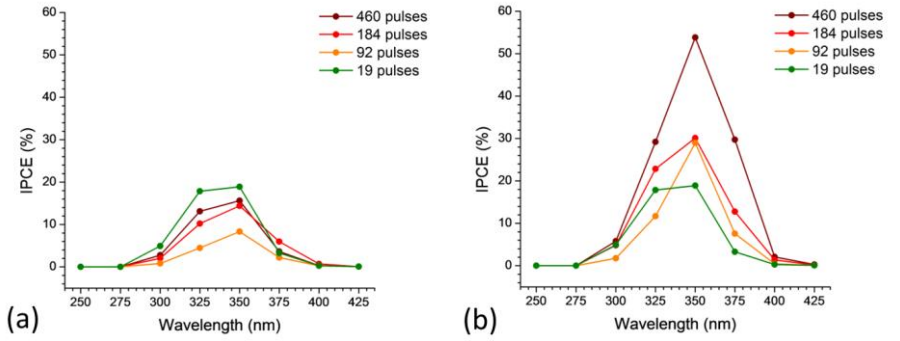

Figure S9: IPCE measured at a constant applied potential of 1.23 V_{RHE} in 1 M NaOH (pH = 13.6) for a series of TiO_2 samples under back irradiation (a) before and (b) after annealing.

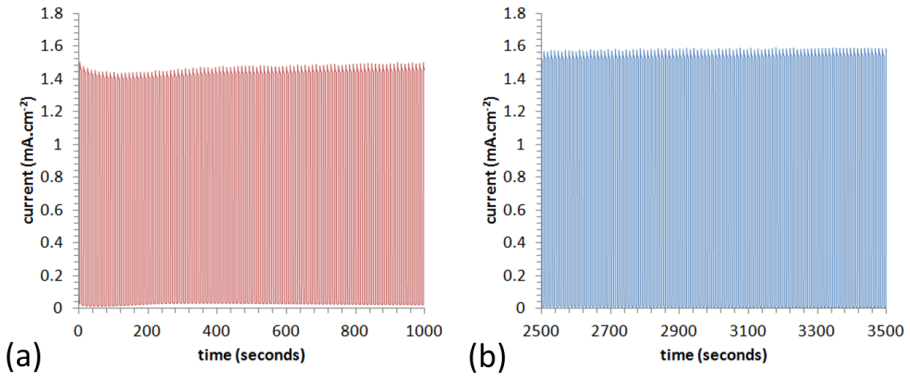

Figure S10: 1 hr stability test, holding the sample made from 92 deposition pulses at 1.23 V_{RHE} and measuring the photocurrent under chopped irradiation, when irradiating the sample from the back with a 365 nm LED (~44 $mW.cm^{-2}$): (a) the performance over the first 15 minutes and (b) last 15 minutes of the test.